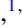







Unified approach to cyclotron and plasmon resonances in a periodic two-dimensional GaAs electron gas hosting the Hofstadter butterfly

Vidar Gudmundsson ^{1,*} Vram Mughnetsyan ^{2,†} Nzar Rauf Abdullah ^{3,4} Chi-Shung Tang ^{5,‡}
Valeriu Moldoveanu ^{6,§} and Andrei Manolescu ^{7,||}

¹Science Institute, University of Iceland, Dunhaga 3, IS-107 Reykjavik, Iceland

²Department of Solid State Physics, Yerevan State University, Alex Manoogian 1, 0025 Yerevan, Armenia


³Physics Department, College of Science, University of Sulaimani,
Kurdistan Region, Iraq

⁴Computer Engineering Department, College of Engineering, Komar University of Science and Technology,
Sulaimani 46001, Kurdistan Region, Iraq

⁵Department of Mechanical Engineering, National United University, Miaoli 36003, Taiwan

⁶National Institute of Materials Physics, PO Box MG-7, Bucharest-Magurele, Romania

⁷Department of Engineering, Reykjavik University, Menntavegur 1, IS-102 Reykjavik, Iceland

 (Received 16 December 2021; revised 21 March 2022; accepted 29 March 2022; published 7 April 2022)

We present theoretical calculations for the cyclotron resonance and various magnetoplasmon modes of a Coulomb interacting two-dimensional GaAs electron gas (2DEG) modulated as a lateral superlattice of quantum dots subjected to an external perpendicular constant magnetic field. We use a real-time excitation approach based on the Liouville–von Neumann equation for the density operator, that can go beyond linear response delivering information of all longitudinal and transverse collective modes of interest to the same order. We perform an extensive analysis of the coexisting collective modes due to the lateral confinement and the magnetic field for a different number of electrons in each dot. In the limit of vanishing dot modulation of the 2DEG we find signs of the structure of the Hofstadter butterfly in the excitation spectra.

DOI: [10.1103/PhysRevB.105.155302](https://doi.org/10.1103/PhysRevB.105.155302)

I. INTRODUCTION

Besides their technological importance, two-dimensional electron systems in semiconductor heterostructures or quantum wells have served as important test beds for advancing the understanding of quantum many-body methods and approaches in condensed matter theory [1]. Fundamental to this is the ability to change their electron density or modulate it spatially into arrays of quasi-one- or zero-dimensional electron systems. The spatial and dynamical reduction of dimensions by external electric and magnetic fields or microstructuring of the semiconductors modifies strongly the effective interactions of the electrons in the systems and thus their electronic, optical, and transport properties.

The Kohn's theorem, published in 1961, states that the energy of the cyclotron resonance of electrons in a uniform external magnetic field is independent of their mutual interactions if the system is placed in a homogeneous rotating microwave field [2]. In the early 1990s this result was extended to explain the two absorption lines appearing in FIR-infrared spectroscopy of parabolically confined quantum dots, and the one line observed in quantum wires, in a homogeneous

external magnetic field [3–6]. It was shown that in the dot system the two lines are due to the rigid oscillations of the center of mass of the electron system with the rotation caused by the magnetic field, or against it. The absorption frequencies are thus independent of the number of electrons. In the wire system there is only a linear oscillation of the center of mass in the effective confining potential renormalized by the magnetic field.

Subsequently, many research groups studied the effects of deviations from the parabolic confinement or the circular shape in individual dots [7–11] and wires [12,13], or in arrays of them [14–19], just to mention a few groups that modeled or measured the FIR absorption of these systems.

The 2DEG in a perpendicular homogeneous magnetic field and a periodic lateral superlattice is known for its fractal energy spectrum, the Hofstadter butterfly [20–23]. The screening of this spectrum has been investigated at the Hartree level [24], and its presence in the FIR-infrared absorption of the system has been investigated with this screening included in the model [25,26].

The FIR absorption of confined or periodically modulated electron systems has mostly been modeled with the density-density response function of linear response [27], but in order to capture the cyclotron resonance or more general transverse collective modes one needs to resort to the current-current response function. The cyclotron resonance has been explored for magnetopolarons in parabolic quantum dots, where Kohn's theorem is broken by the interactions with the phonon modes of the lattice [28], or by interactions with fluctuations and

*vidar@hi.is

†vram@ysu.am

‡cstang@nuu.edu.tw

§valim@infim.ro

||manoles@ru.is

impurities [29,30], or in magnetically confined quantum dots [31].

Comparison of experimental results and models of the cyclotron resonance have shown the importance of including many-body effects in the models [32,33]. Measurements of the cyclotron resonance in high mobility 2DEGs are known for bringing into question the properties of this fundamental excitation mode, especially when interacting with other modes [34], or in more complex experimental setups, with reflection spectroscopy in a terahertz band [35], or in combination with transport measurements in low density and mobility samples under millimeter-wave irradiation [36].

A multitude of different approaches have been used to explore the time evolution of electron systems subjected to short or periodic external excitations, but what makes the linear response or the real-time excitation, described through the Liouville–von Neumann (LvN) equation, appealing is that in both approaches it is acknowledged that the external perturbation drives the electron system out of equilibrium.

Here we want to present a unified approach that can concurrently describe the excitation of the longitudinal collective modes, the plasmons, and the transverse modes, the cyclotron resonances and transverse plasmons, in periodically laterally modulated 2DEG in a homogeneous external magnetic field. We will use the LvN equation for a Hartree interacting 2DEG with a dot modulation, i.e., in a periodic square array of quantum dots, to investigate the time evolution of the system after it is excited with a short terahertz pulse with linear or circular polarization. The mathematical stability of this approach has been studied by Arnold *et al.* [37], and it has been used to investigate various excitation spectra of confined systems in magnetic field for excitation strength beyond linear response [38,39].

The external magnetic field and the confinement potentials mix up the longitudinal and the transverse collective modes and we will also explore their evolution as the modulation vanishes, when the system changes from an array of quantum dots to a periodic 2DEG with vanishing modulation.

We will compare the results for the density oscillations to corresponding results obtained via the conventional linear response. Our “real-time” approach could furthermore be used to access nonlinear response of the system, and as the excitation is with a short temporal pulse it allows us to model terahertz pump-and-probe approaches.

In Sec. II we present the model for the static system, and show how the time evolution of it is found after the excitation with an electrical pulse. In the Sec. III we present the results of the calculations and make a comparison with earlier approaches. In Sec. IV we draw our conclusions.

II. MODEL

A. Time-independent properties

We explore the dynamics of electrons in a square superlattice of quantum dots, shown in Fig. 1, described by the potential

$$V_{\text{per}}(\mathbf{r}) = V_0 \left[\sin\left(\frac{g_1 x}{2}\right) \sin\left(\frac{g_2 y}{2}\right) \right]^2, \quad (1)$$

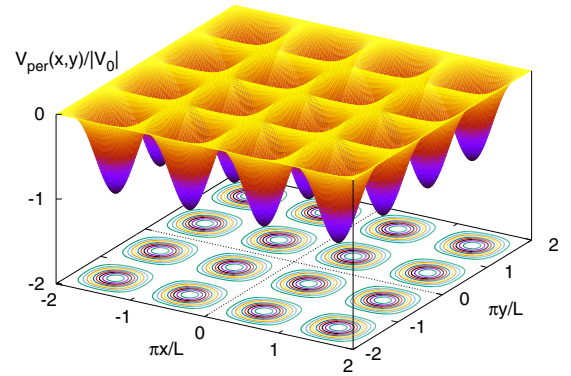


FIG. 1. The periodic potential $V_{\text{per}}(\mathbf{r})$ [Eq. (1)] describing a square lattice of quantum dots with lattice length $L = 100$ nm.

with $V_0 = -16.0$ meV. The lattice is spanned by the lattice vectors $\mathbf{R} = n\mathbf{l}_1 + m\mathbf{l}_2$, with $n, m \in \mathbf{Z}$, and the unit vectors are defined as $\mathbf{l}_1 = L\mathbf{e}_x$ and $\mathbf{l}_2 = L\mathbf{e}_y$. The inverse lattice is spanned by $\mathbf{G} = G_1\mathbf{g}_1 + G_2\mathbf{g}_2$ with $G_1, G_2 \in \mathbf{Z}$, and the unit vectors are

$$\mathbf{g}_1 = \frac{2\pi\mathbf{e}_x}{L} \quad \text{and} \quad \mathbf{g}_2 = \frac{2\pi\mathbf{e}_y}{L}, \quad (2)$$

with $L = 100$ nm.

The Hamiltonian of the Hartree-interacting electrons in the periodic potential (1) and an external homogeneous perpendicular magnetic field is

$$H = H_0 + V_H + V_{\text{per}}, \quad (3)$$

where H_0 is

$$H_0 = \frac{1}{2m^*}\pi^2, \quad \text{with} \quad \pi = \left(\mathbf{p} + \frac{e}{c}\mathbf{A} \right). \quad (4)$$

We use a symmetric gauge for the vector potential, $\mathbf{A} = (B/2)(-y, x)$ [25,40,41] in order to make analytical calculations for the time-dependent excitation of the system more transparent analytically as the cartesian x and y coordinates appear in a similar fashion in the natural eigenfunction basis introduced below. The Hartree Coulomb interaction is

$$V_H(\mathbf{r}) = \frac{e^2}{\kappa} \int_{\mathbf{R}^2} d\mathbf{r}' \frac{\Delta n(\mathbf{r}')}{|\mathbf{r} - \mathbf{r}'|}, \quad (5)$$

with $\Delta n(\mathbf{r}) = n(\mathbf{r}) - n_b$, where $+en_b$ is the average background charge density residing in the plane of the 2DEG and is needed to keep the total system charge neutral (the average charge density of the ions in the crystal lattice). For GaAs we assume $\kappa = 12.4$, and the effective mass $m^* = 0.067m_e$. The mean number of electrons in each dot is noted by N_e .

The external homogeneous magnetic field $\mathbf{B} = B\mathbf{e}_z$ imposes a length scale on the 2DEG in the x - y plane, the magnetic length $l = \{\hbar c/(eB)\}^{1/2}$. At the same time the 2DEG is also under the influence of the lattice length L of the square superlattice. The translation operator $T(\mathbf{R}) = \exp(-i\mathbf{R} \cdot \mathbf{p}/\hbar)$ does not commute with H_0 , $[T(\mathbf{R}), H_0] \neq 0$, but the magnetic translation operator $S(\mathbf{R}) = \exp\{ie/(\hbar c)\chi\}T(\mathbf{R})$ with χ obtained from $T^{-1}\mathbf{A}T = \mathbf{A} + \nabla\chi$ fulfills

$$\begin{aligned} S^{-1}(\mathbf{R})\pi S(\mathbf{R}) &= \pi, \\ S^{-1}(\mathbf{R})\mathbf{r}S(\mathbf{R}) &= \mathbf{r} + \mathbf{R}, \end{aligned} \quad (6)$$

and thus $[S(\mathbf{R}), H_0] = 0$ and $[S(\mathbf{R}), H] = 0$. Nevertheless, generally $[S(\mathbf{R}_1), S(\mathbf{R}_2)] \neq 0$, unless, an integer number of flux quanta $\Phi_0 = hc/e$ flows through the lattice unit cell. This reflects the incommensurability of the two length scales, l and L . We follow Ferrari [40] and Silberbauer [41] introducing a sublattice $\mathbf{c} = l_1/p$ and $\mathbf{d} = l_2/q$ with $p, q \in \mathbb{N}$, where only one flux quantum Φ_0 flows through the primitive unit cell of the sublattice, to construct the eigenfunctions of H_0 ,

$$\phi_{n_l}^{\mu\nu}(\mathbf{r}) = \frac{1}{\sqrt{pq}} \sum_{n,m=-\infty}^{\infty} [S(\mathbf{c})e^{-i\mu}]^m [S(\mathbf{d})e^{-i\nu}]^n \phi_{n_l}(\mathbf{r}), \quad (7)$$

where

$$\phi_{n_l}(\mathbf{r}) = \frac{1}{\sqrt{2\pi l^2 n_l!}} \left(\frac{x+iy}{\sqrt{2}l} \right)^{n_l} \exp\left(-\frac{r^2}{4l^2}\right), \quad (8)$$

with the Landau level number $n_l = 0, 1, 2, \dots$ and $\mu = (\theta_1 + 2\pi n_1)/p$, $\nu = (\theta_2 + 2\pi n_2)/q$, where $n_1 \in I_1 = \{0, \dots, p-1\}$, $n_2 \in I_2 = \{0, \dots, q-1\}$, and $\theta_i \in [-\pi, \pi]$. The eigenfunctions of H_0 (7) form a complete orthonormal Hilbert space $\mathcal{H}_{\theta_1, \theta_2}$, if $(\mu, \nu) \neq (\pi, \pi)$ for all $(n_1, n_2) \in I_1 \times I_2$. The eigenfunctions (7) have to be normalized on a primitive unit cell of the direct lattice with

$$\begin{aligned} \|\phi_{n_l}^{\mu\nu}(\mathbf{r})\|^2 &= \sum_{n,m=-\infty}^{\infty} (-1)^{mn} e^{i(\mu m + \nu n)} \\ &\times \exp\left(-\frac{1}{4l^2}|m\mathbf{d} + n\mathbf{c}|^2\right). \end{aligned} \quad (9)$$

The states of the Hamiltonian H [Eq. (3)] are determined self-consistently within the Hilbert space of the orthonormal eigenfunctions of H_0 [Eq. (4)] with the condition that they remain orthogonal throughout the iterations in accordance with the usual methodology applied in the Hartree approximation.

The primitive unit cell in the direct lattice will be noted by \mathcal{A} . Its area will also be noted by $\mathcal{A} = L^2$ for the square lattice and the number of magnetic flux units through it is $pq = B\mathcal{A}/\Phi_0$.

B. Real-time excitation

For the time-independent mean-field description of electrons in a two-dimensional doubly periodic problem we used a basis of states $|\alpha\rangle = |\mu, \nu, n_l\rangle$ living in each point (θ_1, θ_2) of the magnetic Brillouin zone (MBZ). Due to the properties of the electron-electron Coulomb interaction the same could be stated for the interacting mean-field states $|\alpha\rangle$. Note here that $\langle \mathbf{r} | \alpha \rangle = \phi_{n_l}^{\mu\nu}(\mathbf{r})$. An external time-dependent electric field pulse with circular polarization, or its potential

$$\begin{aligned} V^{\text{ext}}(\mathbf{r}, t) &= V_1 \{ (\Gamma t)^2 e^{-\Gamma t} \} [\cos(k_y y) \cos(\Omega t) \\ &+ c_r \cos(k_x x) \sin(\Omega t)], \end{aligned} \quad (10)$$

with $c_r = \pm 1$ breaks this symmetry and mixes up states at different points, (θ_1, θ_2) in the MBZ, as the wave vectors k_x and k_y are generally neither commensurate with L nor l . We need a larger Hilbert space with states $|\alpha\theta\rangle$ with $\theta = (\theta_1, \theta_2)$, and as the periodic 2DEG is infinite in extent, we have a Hilbert

space of continuous states grouped into discrete energy bands, a rigged Hilbert space [42].

As the eigenfunctions of H_0 [Eq. (4)] $\phi_{n_l}^{\mu\nu}$ and H [Eq. (3)] ψ_α both live at a definite point in the MBZ, we can express their translation as

$$\psi_{\alpha\theta}^*(\mathbf{x} + \mathbf{R}) \psi_{\beta\theta'}(\mathbf{x} + \mathbf{R}) = \{ e^{in(\theta_1 - \theta'_1) + im(\theta_2 - \theta'_2)} \} \psi_{\alpha\theta}^*(\mathbf{x}) \psi_{\beta\theta'}(\mathbf{x}), \quad (11)$$

where we add a reference to the $\theta = (\theta_1, \theta_2)$ point of the MBZ. The Hartree-interaction (5) does not break this symmetry as it is only a functional of the periodic electron density. We will now consider the wave function $\psi_{\alpha\theta}(\mathbf{r}) = \langle \mathbf{r} | \alpha\theta \rangle$ and define the inner product of two Hartree-interacting states in the periodic potential and the extended Hilbert space as

$$\begin{aligned} (\alpha\theta | \beta\theta') &= \int_{\mathbf{R}^2} d\mathbf{r} \psi_{\alpha\theta}^*(\mathbf{r}) \psi_{\beta\theta'}(\mathbf{r}) \\ &= \frac{(2\pi)^2}{\mathcal{A}} \delta^G(\theta - \theta') \int_{\mathcal{A}} d\mathbf{x} \psi_{\alpha\theta}^*(\mathbf{x}) \psi_{\beta\theta'}(\mathbf{x}), \end{aligned} \quad (12)$$

where the integral over the entire \mathbf{R}^2 has been folded back into the primitive unit cell of the lattice, and $\delta^G(\theta - \theta')$ is the Dirac δ function periodic with respect to the inverse lattice. Here we use the notation that $\mathbf{r} \in \mathbf{R}^2$, but $\mathbf{x} \in \mathcal{A}$.

The coupling of states between different points in the MBZ also emerges when linear response formalism is used to calculate the response of the system to an external excitation with a finite wave vector [24,43,44], but the straightforward structure of the response function needed can be expressed without a construction of a larger Hilbert space. Here we want to be able to go beyond a linear response formalism [27] by using, without an approximation, the Liouville–von Neumann equation (LvNE)

$$i\hbar \partial_t \rho(t) = [H[\rho(t)], \rho(t)]. \quad (13)$$

It is thus convenient to express the density operator ρ as a matrix in a larger Hilbert space. The LvNE [Eq. (13)] has been used to investigate strong excitation of individual quantum dots in comparison to other methods [38].

The local electron density is evaluated via the density operator through

$$\begin{aligned} n(\mathbf{r}, t) &= \text{Tr}\{\delta(\hat{\mathbf{r}} - \mathbf{r})\rho(t)\} \\ &= \frac{1}{(2\pi)^4} \int_{-\pi}^{\pi} d\theta d\theta' \sum_{\alpha\beta} \psi_{\alpha\theta}^*(\mathbf{r}) \psi_{\beta\theta'}(\mathbf{r}) \rho_{\beta\theta', \alpha\theta}(t), \end{aligned} \quad (14)$$

where the off-diagonal elements in the density operator play an essential role as their contribution to the density conveys the symmetry breaking effects of the external potential (10) on the 2DEG. The length scale imposed by the external excitation potential (10) breaks the symmetry imposed by the two commensurate scales, the magnetic length l , and the lattice length L of the square lattice.

The Hamiltonian in the LvNE (13) is the time-independent Hamiltonian (3) with a time-dependent term added:

$$H(t) = H_0 + H_H + V_{\text{per}} + H_1(t), \quad (15)$$

where $H_1(t)$ stands both for the time-dependent external potential (10) and the residual Coulomb potential, the addition

to the Hartree potential stemming from the self-consistent changes to the electron density inflicted by the time-dependent external excitation. This dynamical correction to the Hartree potential is now time dependent due to it being a functional of the time-dependent density operator $\rho(t)$, see Appendix A. The LvNE is then

$$i\hbar\partial_t\rho_{\alpha\theta,\beta\theta'}(t) = \{E_{\alpha\theta} - E_{\beta\theta'}\}\rho_{\alpha\theta,\beta\theta'}(t) + \frac{1}{(2\pi)^2} \\ \times \sum_{\gamma} \int_{-\pi}^{\pi} d\theta'' \{(\alpha\theta|H_I[\rho]|\gamma\theta'')\rho_{\gamma\theta'',\beta\theta'}(t) \\ - \rho_{\alpha\theta,\gamma\theta''}(t)(\gamma\theta''|H_I[\rho]|\beta\theta')\}. \quad (16)$$

To evaluate the matrix elements in the last terms of the LvNE (13) we need the translation properties of the wave functions (11) and the residual Hartree interaction

$$\delta V_H(\mathbf{r}, t) = \frac{e^2}{\kappa} \int_{\mathbf{R}^2} d\mathbf{r}' \frac{\delta n(\mathbf{r}', t)}{|\mathbf{r} - \mathbf{r}'|}, \quad (17)$$

with

$$\delta n(\mathbf{r}, t) = \Delta n(\mathbf{r}, t) - \Delta n(\mathbf{r}, 0) \\ = n(\mathbf{r}, t) - n(\mathbf{r}, 0), \quad (18)$$

but here we cannot assume $\delta n(\mathbf{r}, t)$ to have the same periodicity as the lattice, like was possible for the time-independent static system.

The translation properties of the wave functions allow the integral over \mathbf{R}^2 to be folded back to an integral over the unit cell \mathcal{A} and the matrix elements for the Hartree term become

$$(\boldsymbol{\mu}\theta|V_H(t)|\nu\theta') = \frac{1}{\mathcal{A}} \sum_{\mathbf{G}} V_H(\mathbf{G} + \tilde{\boldsymbol{\theta}} - \tilde{\boldsymbol{\theta}}', t) \\ \times \int_{\mathcal{A}} d\mathbf{x} e^{i(\mathbf{G} + \tilde{\boldsymbol{\theta}} - \tilde{\boldsymbol{\theta}}') \cdot \mathbf{x}} \psi_{\boldsymbol{\mu}\theta}^*(\mathbf{x}) \psi_{\nu\theta'}(\mathbf{x}), \quad (19)$$

where $\tilde{\boldsymbol{\theta}} = (\theta_1/l_1, \theta_2/l_2)$, $\tilde{\mathbf{k}} = (k_1l_1, k_2l_2)$, and

$$V_H(\mathbf{G} + \mathbf{k}, t) = \frac{2\pi e^2}{\kappa|\mathbf{G} + \mathbf{k}|} \\ \times \frac{1}{(2\pi)^2\mathcal{A}} \sum_{\alpha\beta} \int_{-\pi}^{\pi} d\boldsymbol{\theta} \int_{\mathcal{A}} d\mathbf{x} e^{-i(\mathbf{G} + \mathbf{k}) \cdot \mathbf{x}} \\ \times \psi_{\alpha\theta}^*(\mathbf{x}) \psi_{\beta\boldsymbol{\theta} + \tilde{\mathbf{k}}}(\mathbf{x}) \Delta\rho_{\beta\boldsymbol{\theta} + \tilde{\mathbf{k}}, \alpha\theta}(t). \quad (20)$$

In Eq. (20) a general wave vector $\mathbf{q} = \mathbf{G} + \mathbf{k}$ has been written in terms of a vector in the reciprocal lattice \mathbf{G} , and a residual \mathbf{k} wave vector residing inside the first MBZ (see Appendix A about the numerical implementation).

The matrix elements of the external potential (10) are calculated with an integral over the entire \mathbf{R}^2 with the same backfolding into the unit cell as was employed in Eq. (19) for the matrix elements of the Coulomb potential (17). To analyze the effects of the excitation on the periodic 2DEG we calculate the time-dependent induced electron density $\delta n(\mathbf{r}, t) = n(\mathbf{r}, t) - n(\mathbf{r}, 0)$ and the averages $\langle \hat{O} \rangle = \text{Tr}\{\hat{O}\rho(t)\}$ for the dipole operators $\hat{O} = \hat{x}$ and $\hat{O} = \hat{y}$, the quadrupole operator $\hat{O} = \hat{y}\hat{x} - \langle \hat{y} \rangle \langle \hat{x} \rangle$, and the monopole operator $\hat{O} = \hat{x}^2 + \hat{y}^2 - \langle \hat{x} \rangle^2 - \langle \hat{y} \rangle^2$, where the matrix elements of \hat{O} are evaluated with a spatial integral over just one unit cell. Defined in this way the

last two operators are the relative quadrupole and monopole operators for the case of $N_e = 1$ in an individual isolated quantum dot [45]. The average for the quadrupole operator we indicate with Q_2 and use Q_0 for the monopole operator. All the aforementioned averages can be used to explore and quantify collective modes with density variations, in order to detect rotational collective modes (transverse modes) we need to gauge modes, where the current density $\mathbf{j} = -e\dot{\mathbf{r}} = -(ie/\hbar)[H(t), \mathbf{r}]$ plays a role [38]. This will be accomplished by calculating the dimensionless quantity

$$Q_j = \frac{1}{l^2\omega_c} (i(\mathbf{r} \times \dot{\mathbf{r}}) \cdot \hat{\mathbf{z}}), \quad (21)$$

which is directly proportional to the orbital part of the magnetization measured in one cell, or the orbital angular momentum in the cell.

III. RESULTS

For the real-time excitation with a linear polarization we use the external potential

$$V^{\text{ext}}(\mathbf{r}, t) = V_t e^{-\Gamma t} \cos(k_i x_i) \sin(\Omega t), \quad (22)$$

where $k_i x_i = k_x x$ or $k_y y$ depending on whether the polarization is along the x or the y direction in the plane of the 2DEG. Originally (22) was chosen for the excitation with linear polarization, and modified and extended to circular polarization as (10) in order to have the excitation always starting from 0 at $t = 0$.

To understand the nature of the confining dot potential, we can consider a polar coordinate system with origin at the minimum of the periodic potential (1) in one cell. An expansion to the fourth order around the minimum gives

$$V_{\text{per}}(x, y) \approx V_0 \left[\left(\frac{\pi^2}{L^2} \right) r^2 - \left(\frac{\pi^4}{12L^4} \right) r^4 \left\{ 1 + \frac{3 \sin^2(2\theta)}{2} \right\} - 1 \right], \quad (23)$$

if $r \ll L$. The parabolic part of the expansion (23) would lead to a confinement energy $\hbar\omega_0 \approx 6.0$ meV. As expected the fourth order term describes a weakening of the confinement potential, and a square symmetric deviation from the circular shape at low energy. As the energy is increased the shape of the square lattice takes over.

If the magnetic field is increased (the number of flux quanta through the unit cell pq) the magnetic length l becomes smaller compared to the lattice length L and an electron in the lowest state becomes better localized in the dot potential (1). The magnetic length l is then a convenient parameter to compare to the potential in Fig. 2 in order to determine the degree of deviation from parabolic confinement felt by an electron.

A. Comparison to linear response

To compare to the results of the real-time excitation of the system we use the linear response model developed earlier for the absorption $P(\omega)$ [24] using $n_l = 10$ as the number of Landau levels and a 32×32 grid of unevenly spaced (θ_1, θ_2) points for the unit cell in the reciprocal lattice for a repeated four-point Gaussian quadrature. In order to smear out the

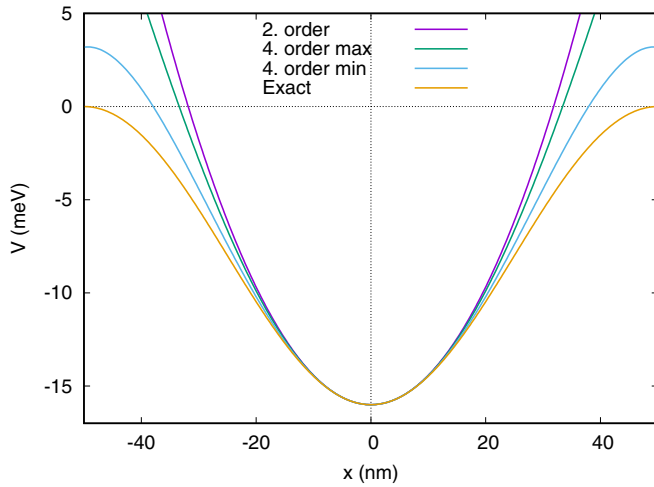


FIG. 2. The confinement potential defining the dot in each unit cell as seen along the x axis close to their center. Compared are the exact potential (orange), the second order expansion from Eq. (23) (violet), and the fourth order (green) along $\theta = 0 + n\pi$, and the fourth order along $\theta = \pi/4 + n\pi$ (blue), with $n = 0, 1, 2, 3 \dots$. The difference between the max ($\theta = 0 + n\pi$) and the min ($\theta = \pi/4 + n\pi$) fourth order expansions gives an indication of the deviation from circular symmetry imposed by the square lattice.

effects of the singularities in the response functions, we use a constant broadening $\hbar\eta = 0.2\hbar\omega_c$. The large broadening is necessary as the lowest states in the dots are well localized forming very narrow energy bands in the lattice. For the real-time excitation we employ an 8×8 equally spaced grid in the reciprocal unit cell in combination with a repeated Booles quadrature and no level broadening. Furthermore, we use $n_l = 10$ for the static part of the calculation, but limit the number of Landau bands used in the calculation of the time evolution to $n_{\text{Ht}} = 8$. Here we are not aiming at exploring the response of the system far beyond the linear response regime, and we have tested the convergence of the results for the strength selected for the excitation.

In Fig. 3 we compare $P(\omega)$ for dipole excitations in the linear response model with the Fourier power spectrum for the mean values $\langle x \rangle$ and $\langle y \rangle$ for the real-time excitation for three values of the magnetic flux pq through the unit cell. In all the calculations we use linear polarization of the excitation with a very low impulse $k_x L$ or $k_y L$ in order to explore the Kohn modes for one electron in each quantum dot in the array [2,4,8,46]. No significance should be given to the change in relative height of the main peaks in the real-time excitation as that simply depends on the frequency distribution offered to the system by the shape of the excitation pulse used. Here we have taken care of not including too high frequency in the pulse. In the real-time excitation no broadening is assumed, but the length of the time series gives the peaks in the Fourier power spectrum an apparent width. With few exceptions we have calculated the time series with 10 200 steps of length 0.02 ps each.

The magnetic length $l \approx 19.9$ nm for $pq = 4$, 28.2 nm for $pq = 2$, and 39.9 nm for $pq = 1$, and consequently, though not shown here, the overlap of the electron density is very small for $N_e = 1$ at $pq = 4$, but considerable for $pq = 1$, and

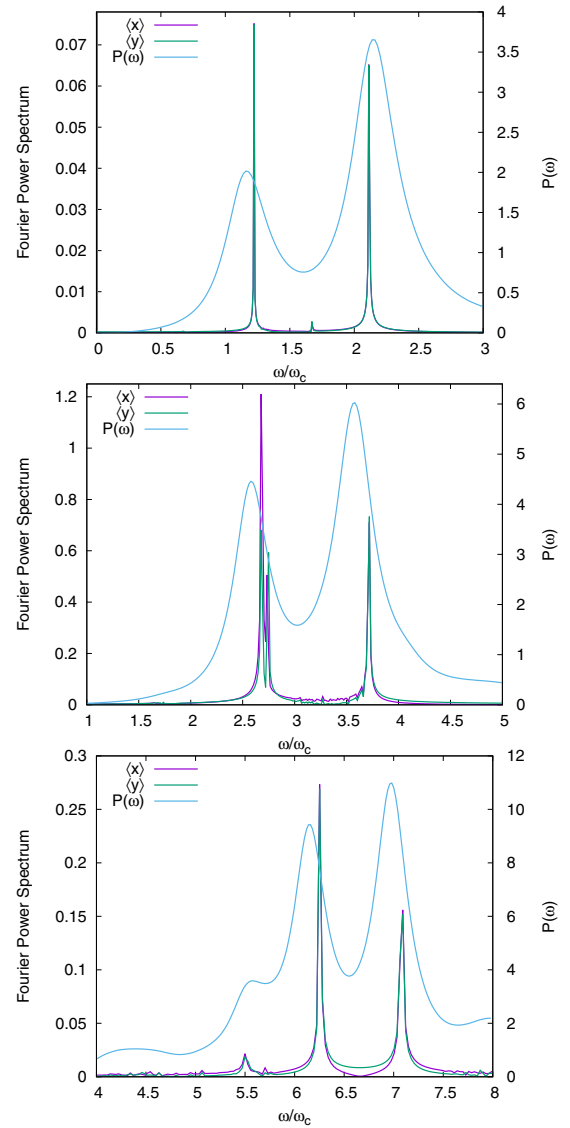


FIG. 3. Comparison of the Fourier power spectra for $\langle x \rangle$ and $\langle y \rangle$ for linearly polarized excitation of a rectangular array of quantum dots with the linear response absorption $P(\omega)$ for the same system for $pq = 4$ (top), $pq = 2$ (center), and $pq = 1$ (bottom). In the linear response calculation the broadening in the response function is $\hbar\eta = 0.2\hbar\omega_c$ and $k_x L = k_y L = 0.01$. In the real-time excitation $k_x L = 0.0001$, $k_y L = 0$, and $V_l = 0.01$ meV for $pq = 4$ and $pq = 1$, but $V_l = 0.1$ meV for $pq = 2$. $N_e = 1$, $V_0 = -16$ meV, $L = 100$ nm, $T = 1.0$ K, $\hbar\Gamma = 4.0$ meV, and $\hbar\Omega = 4.5$ meV.

not large, but not negligible for $pq = 2$. Accordingly, we see in Fig. 3 for $pq = 4$ (upper panel) rather clean two Kohn peaks. For $pq = 2$ (center panel) we see two Kohn peaks, but the lower one shows a small splitting caused by a slight influence of the square symmetry of the lattice at this magnetic flux [11]. At still lower flux $pq = 1$ (bottom panel) the splitting of the lower peak is clearly visible.

Not shown here, but a graph of $\langle y \rangle$ versus $\langle x \rangle$ shows an extremely simple pattern for the center of mass (CM) motion known for circular parabolically confined quantum dots for $pq = 4$, but with some slight modulation for $pq = 3$, that is

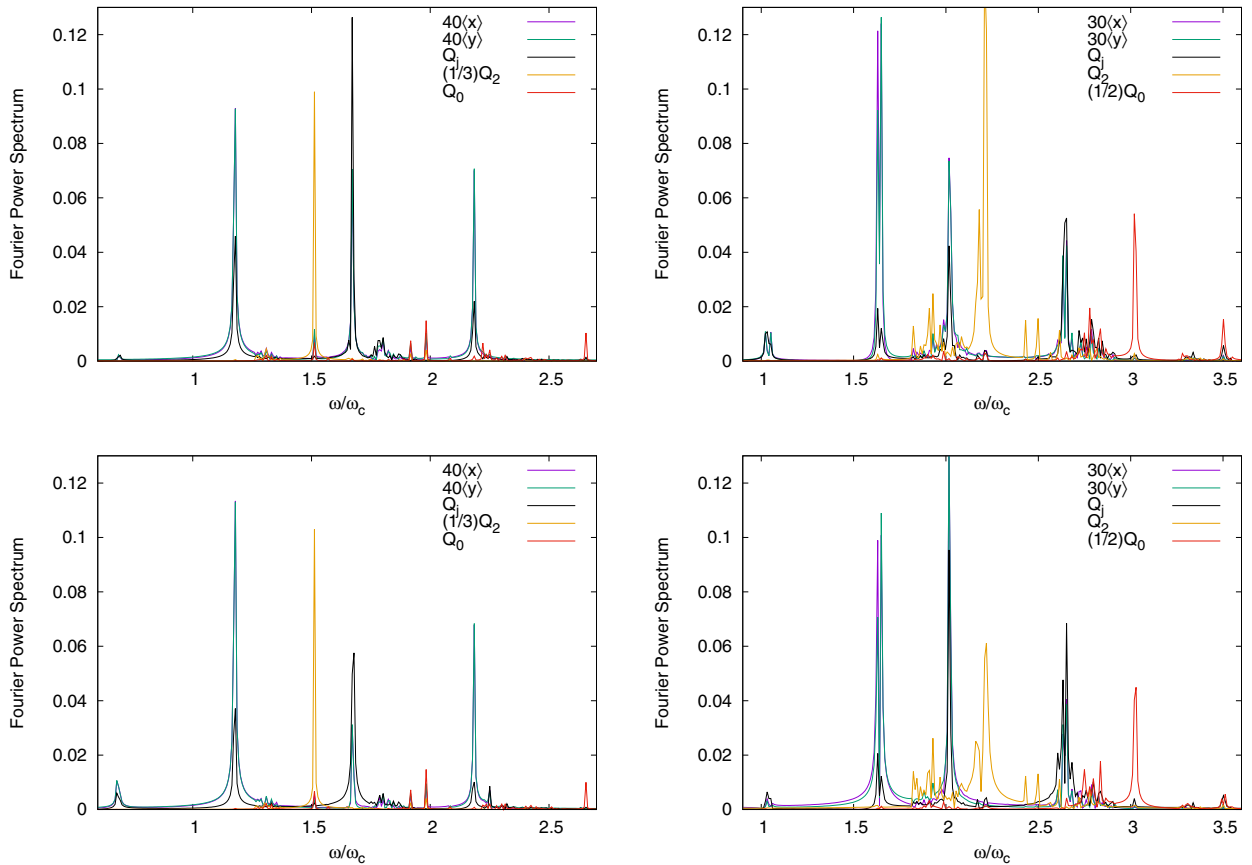


FIG. 4. The Fourier power spectra for a rectangular array of quantum dots for $pq = 4$, $c_r = +1$ (left, top), $pq = 3$, $c_r = +1$ (right, top), $pq = 4$, $c_r = -1$ (left, bottom), and $pq = 3$, $c_r = -1$ (right, bottom) for $N_c = 1$, $k_x L = k_y L = 0.785$, $V_t = 0.001$ meV, $V_0 = -16$ meV, $L = 100$ nm, $T = 1.0$ K, $\hbar\Gamma = 1.5$ meV, and $\hbar\Omega = 4.5$ meV.

increased for $pq = 2$. For $pq = 1$ the simplicity is lost, but the pattern is still very regular.

The deviation from parabolic confinement of the dots does affect their excitation spectra. Roughly estimated, the redshift caused by the nonparabolicity is 0.5 meV for $pq = 4$, 1.1 meV for $pq = 2$, and 1.8 meV for $pq = 1$. This nonparabolic redshift applies equally to both methods of calculations. There is a slight deviation between the results of both methods. To the largest extent, this is a redshift for the linear response results caused by the large level broadening needed due to the flat bands produced by the low levels in the dots. A clear exception to this is the upper Kohn peak for $pq = 4$ in Fig. 3(a), where a complex interaction with a classical Bernstein mode around $\omega/\omega_c = 2$ takes place [12,47]. In addition, we have to keep in mind that the linear response calculation includes dipole and all higher modes like quadrupole modes that are not shown here for the real-time excitation, and due to the large broadening in the linear response we cannot resolve a possible fine structure of the broad peaks.

For collective density modes comprised of dipole active transitions in arrays of quantum dots in a magnetic field the real-time excitation method results in higher resolution of the mode spectrum as no broadening has to be assumed for the underlying single-electron states of the system. The total energy is strictly conserved in the real-time excitation after the pulse has died out, but in linear response nothing can be stated

about the energy conservation since the results are linear in the excitation potential.

A slightly different approach to real-time excitation of a single quantum dot with Hartree-Fock interacting electrons has been compared to results obtained via linear response for the corresponding system [45,48].

B. Extended mode spectrum for quantum dots

Deviations from circular shape and parabolic confinement of individual dots in the array and excitation of the system with pulses that carry a wave vector supplying an impulse to it makes it important to investigate the mode spectrum in the relevant energy range. The linear response built on the density-density response function can supply information about dipole and quadrupole collective density modes and in some special situations the monopole or breathing mode (longitudinal modes), but the external magnetic field can lead to collective current modes (transverse modes) that need to be examined through the current-current response function. In the real-time excitation method all these modes can become active and their “detection” depends on the expectation values of which operators are registered through the time evolution of the system.

This is done in Fig. 4 for an excitation pulse with circular polarization (10) as it is particularly well suited to excite

collective current modes in an external magnetic field. In Fig. 4 the Fourier power spectra for the expectation values of the monopole operator Q_0 , the dipole operators $\langle x \rangle$ $\langle y \rangle$, the quadrupole operator Q_2 , and the current operator Q_j are displayed. These operators are all introduced in Sec. II, just before and with Eq. (21). The results are presented for both directions of the circular polarization $c_r = \pm 1$. For $pq = 4$ in the left panels of Fig. 4 we note the Q_1 ($\langle x \rangle$ and $\langle y \rangle$) Kohn peaks at $\omega/\omega_c \approx 1.18$ and 2.18 and in the same location peaks representing current excitations Q_j . Exactly in between the Kohn peaks is a peak for Q_j at $\omega/\omega_c \approx 1.68$, below which is a strong quadrupole peak at $\omega/\omega_c \approx 1.5$. Clearly the strength of the Q_j peaks depends on the direction of the circular polarization c_r . The main Q_j peak at $\omega/\omega_c \approx 1.68$ is essentially a manifestation of the cyclotron resonance in a quantum dot made possible by the breaking of the Kohn theorem by the confinement potential and the external impulse delivered by the excitation pulse. The location of the lower quadrupole peak (the one seen here) is in accordance with the results shown in Fig. 4 in Ref. [8], and in Fig. 2 in Ref. [49].

Wilson *et al.* published a simple classical model of the cyclotron resonances of a parabolically confined electron in a homogeneous magnetic field, in an article exploring possible electron phases in an Si inversion layer in a strong magnetic field [50]. They identify two cyclotron modes, the low energy anticyclotron mode ω_1 made possible by the parabolic confinement potential, and the normal cyclotron resonance ω_2 . With our parameters here, estimating $\hbar\omega_0 \approx 6.0$ meV, this classical model for the flux $pq = 4$ gives $\omega_1/\omega_c \approx 1.66$ and $\omega_2/\omega_c \approx 2.66$. The lower mode is very close to the main cyclotron mode seen in the left panels of Fig. 4, and for $pq = 3$ the lower peak is at $\omega_1/\omega_c \approx 2.34$ compared to ≈ 2 in the right panels of Fig. 4. The larger deviation for the lower flux, $pq = 3$, is expected as then the effective confinement is farther away from the parabolic case. The higher mode, the usual cyclotron mode, of the classical model does probably have a low strength due to the rather high confinement that makes the classical model inadequate, and we notice instead that both Kohn peaks have a contribution from the Q_j excitation. The confinement potential and the magnetic field are mixing the purely longitudinal and transverse collective modes.

The right panels of Fig. 4 show the Fourier power spectra for $pq = 3$. Still we can identify the Kohn dipole peaks and the quadrupole peak that is now located just above the cyclotron resonance peak at $\omega/\omega_c \approx 2$.

Important is to notice that generally the cyclotron, the quadrupole, and the monopole modes are much stronger activated by the circularly polarized excitation pulse than the dipole modes. This reflects the strong role of the external magnetic field. With increasing magnetic field, and thus pq , the excitation with circular polarization is more effective in exciting rotational modes.

In a usual setup of FIR-absorption experiments the wave vector or the impulse is very small as the wavelength of the radiation is much larger than the lattice length $L = 100$ nm, but in Raman scattering measurements and in modeling thereof the system is excited with a larger wave vector [51–54], as the radiation is inelastically scattered of the electron system.

A single electron in an isolated quantum dot would not be well described by the Hartree approximation, but here is

important to have in mind that one electron in a quantum dot feels the influence of the electrons in the neighboring unit cells. With our selected parameters each electron feels the influence of 25 electrons. Its self-interaction is reduced by the positive charge background representing the ions in the crystal. Before going to lower magnetic fields we show in Fig. 5 how the excitation spectrum changes as the number of electrons is increased in each dot from 1 to 3 and in the bottom right panel how the mean total energy changes. The mean total energy can be compared to the confining potential in Fig. 2 in order to see how the symmetry of the underlying square lattice affects the potential as the number of electrons increases in the dots. Not shown here, but for 1 or 2 electrons in a dot the overlap of the probability density is very small between neighboring dots, but for the case of three electrons the density between the dots reaches 10% of its peaks value.

We note that in the right panels of Fig. 4, and in Fig. 5 for $N_e = 2$ or 3, there appear frequency regions with very many low intensity peaks. This reflects the energy band structure of the quantum dot array and is explained in Appendix B.

We continue with the Fourier power spectra for quantum dots with $N_e = 1$ shown in Fig. 4 for a circularly polarized excitation pulse and observe in Fig. 6 the results for $pq = 2$ (left panels) and $pq = 1$ (right panels). For the lower magnetic flux ($pq = 1$) we see two clear Kohn peaks, where the lower one is clearly split due to the square symmetry of the lattice, and the cyclotron resonance is below the Kohn peaks. For the higher magnetic flux ($pq = 2$) the lower Kohn peak is difficult to resolve clearly due to a fine splitting caused by the lattice and both Kohn peaks interact strongly with cyclotron resonance peaks. Interestingly, the monopole peaks are prominent.

C. The limit to a flat system

The presence of the cyclotron resonance peaks in the excitation spectra for the arrays of quantum dots gives rise the question: What happens when the strength of the modulation defining the dot array $V_0 \rightarrow 0$? Important is to have in mind that even though the modulation is set to vanish the dynamic of the system is not set totally free as the restrictions of periodicity are still imposed on the system in the model. In order to start with results of some familiarity we display the results for the lowest magnetic flux $pq = 1$ for $V_0 = 0$ in Fig. 7. There are small cyclotron resonance peaks at $\omega/\omega_c = 1, 2$, and 3 as expected and for a slightly higher energy split plasmon peaks follow. This situation reminds us of the absorption spectra shown in Fig. 1 in Ref. [24] for linear response. There we see dipole plasmon peaks with increasing oscillator strengths in higher Landau levels as the impulse kL increases with Bernstein-type splitting [12,47]. Here we cannot identify Bernstein modes as $k_x L = 10^{-4}$ and $k_y L = 10^{-4}$ is very low, but due to a higher resolution we can identify higher order plasmon modes. In addition, here we see the cyclotron resonances and further plasmon details as the quadrupole and monopole modes. Even though the excitation pulse here carries a small impulse the periodicity of the systems represents a larger possible impulse, and as the Landau level separation for $pq = 1$ is small the excitation

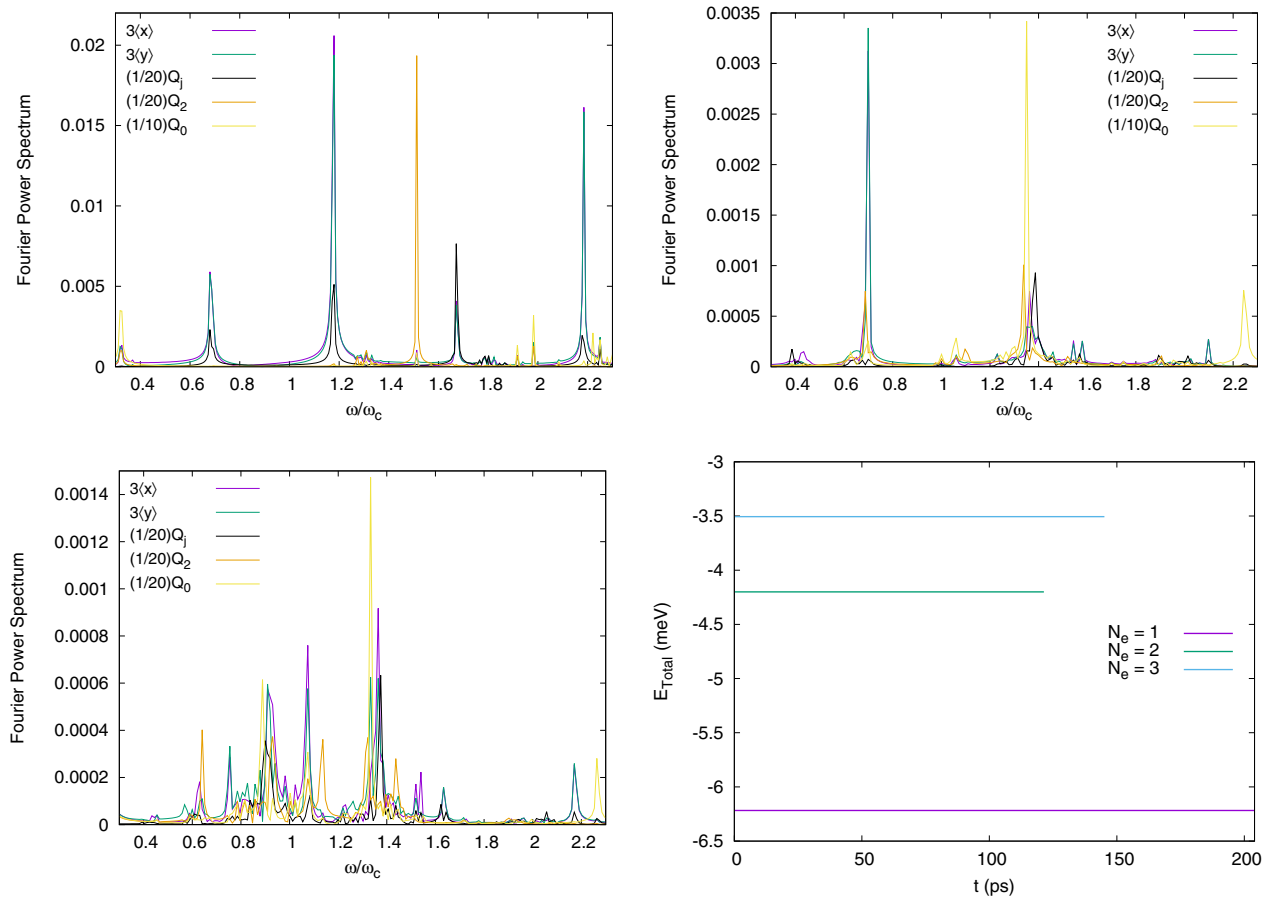


FIG. 5. The Fourier power spectra for a rectangular array of quantum dots for $pq = 4$ and linearly polarized excitation field for $N_e = 1$ and $V_l = 0.01$ meV with $k_x L = 0.785$ and $k_y L = 0$ (left top), $N_e = 2$ and $V_l = 0.001$ meV with $k_x L = 0.524$ and $k_y L = 0$ (right top), $N_e = 3$ and $V_l = 0.001$ meV with $k_x L = 0.524$ and $k_y L = 0$ (left bottom), and the average energy of the system (right bottom). $V_0 = -16$ meV, $L = 100$ nm, $T = 1.0$ K, $\hbar\Gamma = 1.5$ meV, and $\hbar\Omega = 4.5$ meV.

pulse may couple better to higher cyclotron resonances. Not shown here, but there is no essential difference between the spectra for the two directions of circular polarization for the low magnetic field at $pq = 1$.

In Fig. 8 the Fourier power spectra for the higher flux $pq = 3$ are shown for the range $0.9 \leq \omega/\omega_c \leq 1.4$ for a periodic system with vanishing modulation $V_0 = 0$ for a different number of electrons $N_e = 1$ (top), 2 (center), 3 (bottom) and both circular polarizations $c_r = +1$ (left) and -1 (right). For this vanishing modulation at $pq = 3$ each Landau level is threefold degenerate. The spectra in Fig. 8 all show a clear cyclotron fundamental resonance peak with a maximum at $\omega/\omega_c = 1$, and all show a set of threefold plasmon peaks at a higher energy before they become flat. As expected, the plasmon peaks move to higher energy as the number of electrons in a unit cell increases. The structure of spectra is more complex, just above the first cyclotron resonance at $\omega/\omega_c = 1$ there are threefold peaks, and in between the main set of peaks mentioned here, there are two or three peaks still with high quadrupole contribution.

Not shown here, but for the higher flux $pq = 4$ we see sets of three to four peaks appearing in the excitation spectra. Possibly, longer time series for the Fourier analysis would result in clear sets of four peaks.

In Fig. 9 the excitation spectrum for the current excitations Q_j corresponding to the upper left panel of Fig. 8 is repeated for vanishing modulation $V_0 = 0$ together with the results for $V_0 = -0.5$ and -0.1 meV in order to show the stability of the spectra as the modulation approaches 0. Especially, the threefold plasmon peak at the higher energy end of the spectrum is insensitive to the change in the modulation. The “flat top” of the cyclotron resonance peak in Fig. 9 is caused by the limited frequency resolution caused by the length of, and the time step used, in the time series of the averages.

Note that we have not restricted further the Hilbert space in any way for the calculation for the flat system. For the static part we use 11 Landau levels, each split into pq subbands, and for the dynamical part we use at least three Landau levels. We have checked the stability of the results for different sizes of the Hilbert space. Our conclusion is thus that the periodic boundary conditions built on the magnetic translations are a sufficient condition for the appearance of the excitation peak structure or splitting in accordance with the number of subbands in the Landau levels as reflected by the Hofstadter butterfly energy spectrum for a rational number of magnetic flux quanta through a unit cell. Clearly in a physical system the periodicity and the modulation cannot be separated, so we

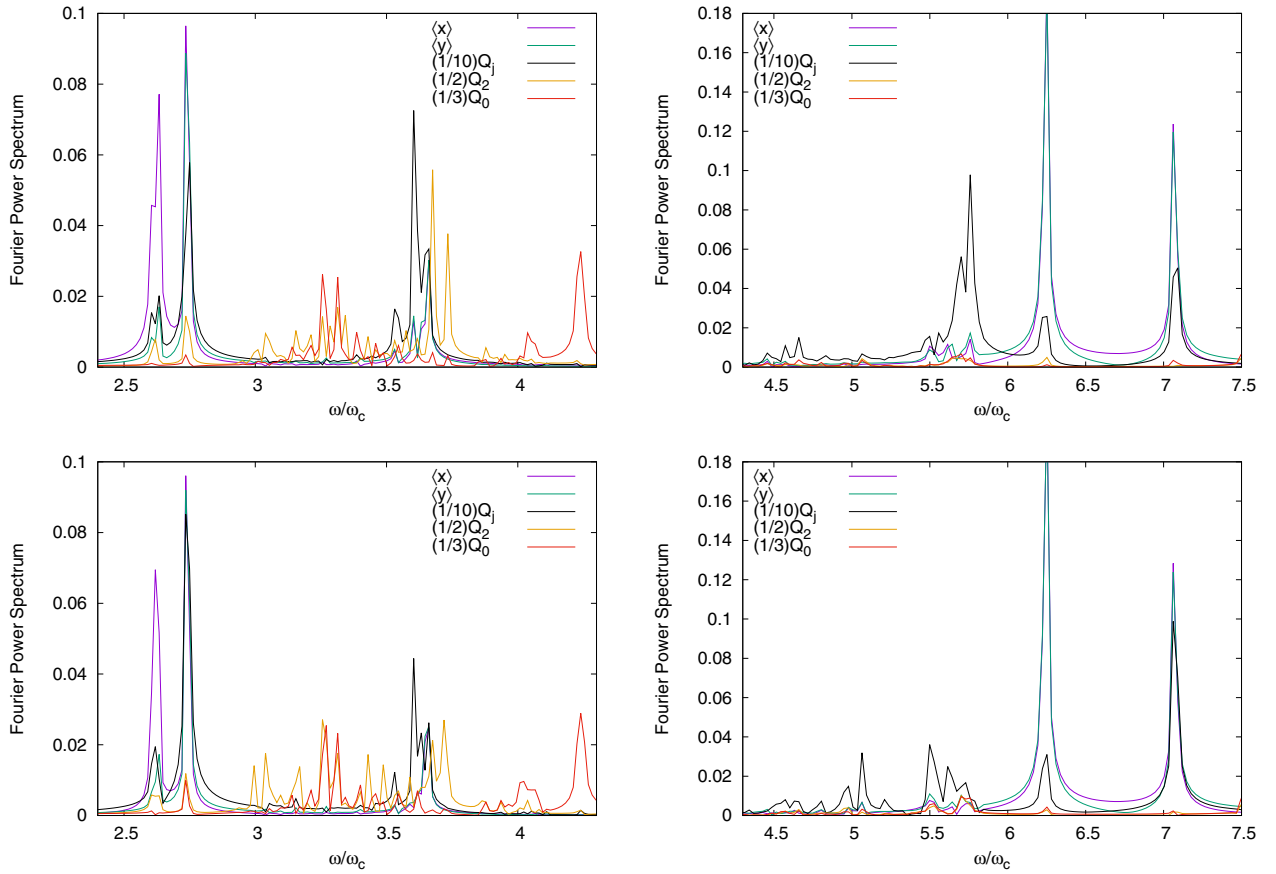


FIG. 6. The Fourier power spectra for a rectangular array of quantum dots for $pq = 2$, $c_r = +1$ (left, top), $pq = 1$, $c_r = +1$ (right, top), $pq = 2$, $c_r = -1$ (left, bottom), and $pq = 1$, $c_r = -1$ (right, bottom) for $N_e = 1$, $k_x L = k_y L = 0.785$ for $pq = 2$, but $k_x L = k_y L = 0.393$ for $pq = 1$, $V_t = 0.001$ meV, $V_0 = -16$ meV, $L = 100$ nm, $T = 1.0$ K, $\hbar\Gamma = 1.5$ meV, and $\hbar\Omega = 4.5$ meV.

adopt the view here that our results describe the system in the limit of vanishing modulation.

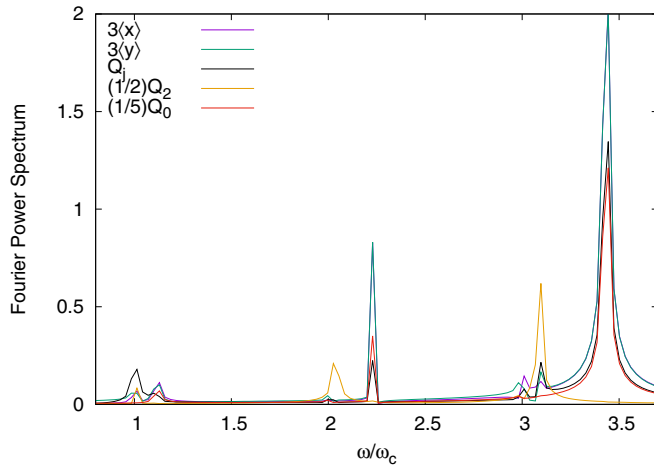


FIG. 7. The Fourier power spectrum for electrons in a rectangular array of flat unit cells for $c_r = +1$, $pq = 1$, for $N_e = 1$, $k_x L = k_y L = 10^{-4}$, $V_t = 0.01$ meV, $V_0 = 0$ meV, $L = 100$ nm, $T = 0.1$ K, $\hbar\Gamma = 1.5$ meV, and $\hbar\Omega = 4.5$ meV. The spectrum for $c_r = -1$ is identical.

IV. CONCLUSIONS

We have demonstrated that a real-time excitation of a modulated 2DEG in a homogeneous perpendicular external magnetic field can be used to explore a wide range of collective modes in the system including longitudinal and transverse modes. This cannot be achieved by the linear response approach if only density-density correlations are considered, but current-current response can lead to the emergence of transverse modes. The external magnetic field with its Lorentz force makes the transverse modes particularly important in the system investigated here. Furthermore, the real-time approach opens the possibility to explore modes beyond the linear response, i.e., nonlinear response, or calculations for pump-and-probe schemes, though that was not done here.

In the calculations here we have checked for each case that the excitation only delivers a tiny amount of energy into the system. This is done in order to have a comparison to earlier calculations, when establishing our method, and in order not to put too large requirement on the Hilbert space needed for the dynamical part of the calculation. We have explored the excitation of a strong breathing mode in a single quantum dot, where different modes do not couple due to the simple symmetry of the system [39]. The band structure of the square dot array here has made the calculational effort, analytically and numerically, much more challenging.

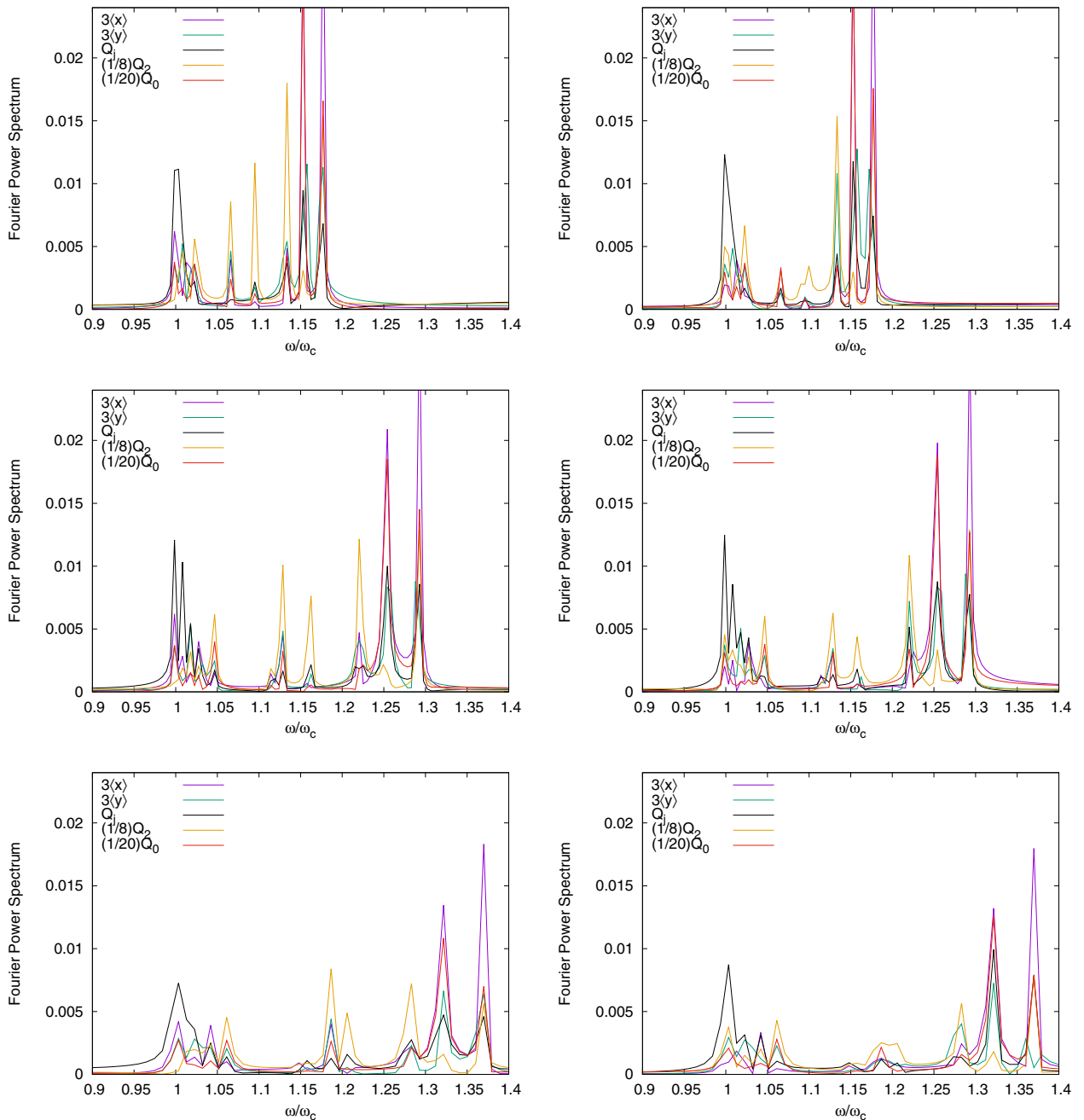


FIG. 8. The Fourier power spectra for electrons in a rectangular array of flat unit cells for $c_r = +1$, $N_e = 1$ (left, top), $c_r = -1$, $N_e = 1$ (right, top), $c_r = +1$, $N_e = 2$ (left, center), $c_r = -1$, $N_e = 2$ (right, center), $c_r = +1$, $N_e = 3$ (left, bottom), and $c_r = -1$, $N_e = 3$ (right, bottom) for $pq = 3$, $k_x L = k_y L = 0.785$, $V_t = 0.001$ meV, $V_0 = 0$ meV, $L = 100$ nm, $T = 1.0$ K, $\hbar\Gamma = 1.5$ meV, and $\hbar\Omega = 4.5$ meV.

We are able to attain information about the cyclotron resonances in an array of quantum dots concurrently with the better known dipole, quadrupole, and monopole plasmon collective modes. The lack of this information has been pointed out by experimental researchers for small electronic systems with confinement that deviates from the parabolic ideal [29].

With the real-time approach we have been able to see how the cyclotron resonances evolve into their well known form as the confinement potential vanishes in the 2DEG. In the flat, but periodic, system we see peak structures for the plasmons and the cyclotron resonances that reflect the underlying degeneracies of the band structure of the Hofstadter butterfly.

We show that this structure of the excitation spectra is rather stable as the modulation of the 2DEG approaches 0, and can be seen for different numbers of electrons in the unit cell.

ACKNOWLEDGMENTS

This work was financially supported by the Research Fund of the University of Iceland, and the Icelandic Infrastructure Fund. The computations were performed on resources provided by the Icelandic High Performance Computing Center at the University of Iceland. V. Mughnetyan and V.G. acknowledge support by the Armenian State Committee of

Science (Grant No. 21SCG-1C012). V. Moldoveanu acknowledges financial support from the Romanian Core Program PN19-03 (Contract No. 21 N/08.02.2019). V. M. acknowledges support by the Armenian State Committee of Science (Grant No. 21T-1C247).

APPENDIX A: INFORMATION ABOUT THE NUMERICAL IMPLEMENTATION

In the dynamic Hartree approximation the Hamiltonian for the system has to be updated in each time step. At a time $t > 0$ the Hamiltonian is

$$H(t) = H_0 + V_{\text{per}} + H^{\text{ext}}(t) + V_H[\Delta n(0)] + \delta V_H[\delta n(t)], \quad (\text{A1})$$

where Eq. (15) has been elaborated, and $\delta n(t) = n(t) - n(0)$. Shortly after, the density can be approximated by

$$\delta n(t + \delta t) = n(t + \delta t) - n(0) \approx \delta n(t) + \delta n(\delta t) \quad (\text{A2})$$

for a very short time step δt with respect to all timescales in the system. Thus, the Hamiltonian at the later time will be

$$H(t + \delta t) = \{H_0 + V_H[\Delta n(0)] + \delta V_H[\delta n(t)]\} + V_{\text{per}} + H^{\text{ext}}(t + \delta t) + \delta V_H[\delta n(\delta t)], \quad (\text{A3})$$

where the terms in the curly bracket on the right side in the first line can be considered as the time updated or renormalized Hamiltonian of the original static system. The effect of the positive homogeneous background charge of the system n_b is to cancel out all terms with $\mathbf{q} = \mathbf{G} + \mathbf{k} = 0$, just like is done for the term with $\mathbf{G} = 0$ in the calculation for the static system.

In order to increase the numerical accuracy for the matrix elements of the dynamical Hartree interaction in Eqs. (19) and (20) the Fourier transform is done after the construction of the variation in the density. This means that we consider the

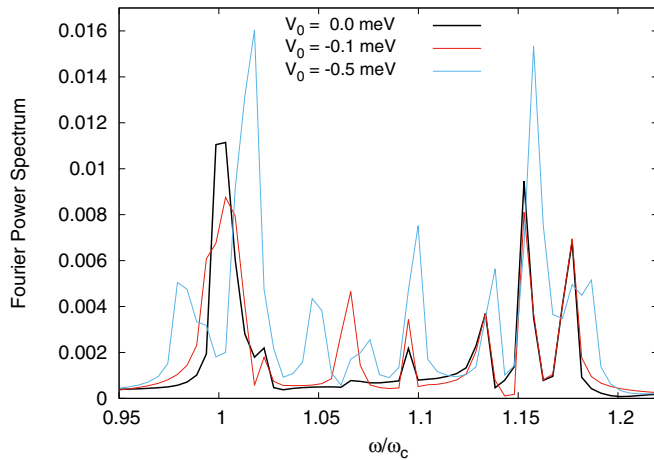


FIG. 9. The Fourier power spectra for current excitations Q_j for electrons in a rectangular array of flat or slightly modulated unit cells with a dot potential for varying degree of modulation V_0 . $N_e = 1$, $pq = 3$, $c_r = +1$, $k_x L = k_y L = 0.785$, $V_i = 0.001$ meV, $L = 100$ nm, $T = 1.0$ K, $\hbar\Gamma = 1.5$ meV, and $\hbar\Omega = 4.5$ meV.

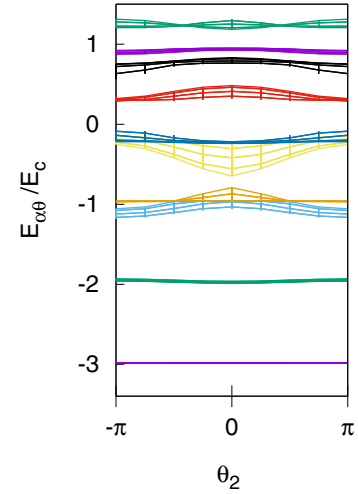


FIG. 10. The structure of the ten lowest energy bands $E_{\alpha\theta}$ projected on θ_2 for $pq = 3$, $N_e = 1$ corresponding to the right panels in Fig. 4. $E_c = \hbar\omega_c$.

integrals

$$\delta n(\mathbf{G} + \mathbf{k}) = \int_A dx e^{i(\mathbf{G} + \mathbf{k}) \cdot \mathbf{x}} \delta n(\mathbf{x}, \mathbf{k}) \quad (\text{A4})$$

and

$$\delta n(\mathbf{x}, \mathbf{k}) = \frac{1}{(2\pi)^2} \sum_{\alpha\beta} \int_{-\pi}^{\pi} d\theta \psi_{\alpha\theta}^*(\mathbf{x}) \psi_{\beta\theta + \mathbf{k}}(\mathbf{x}) \times \Delta\rho_{\beta\theta + \mathbf{k}, \alpha\theta}. \quad (\text{A5})$$

In addition, this approach simplifies the monitoring of symmetries during the calculations.

Integrations over $\mathbf{q} = \mathbf{G} + \mathbf{k}$ in the reciprocal space are divided into sums over the inverse lattice vectors \mathbf{G} and numerical integrations over \mathbf{k} with a equispaced grids constructed from repeated applications of the five point Booles

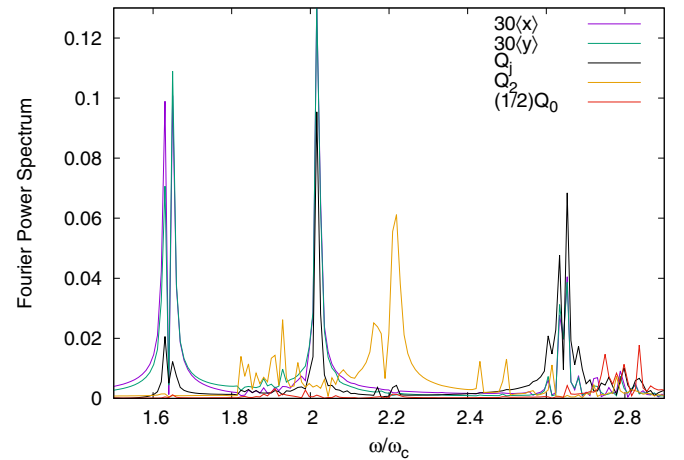


FIG. 11. The Fourier power spectra for a rectangular array of quantum dots for $pq = 3$, $c_r = -1$ for $N_e = 1$, $k_x L = k_y L = 0.785$, $V_i = 0.001$ meV, $V_0 = -16$ meV, $L = 100$ nm, $T = 1.0$ K, $\hbar\Gamma = 1.5$ meV, and $\hbar\Omega = 4.5$ meV. The figure represents a zoom-in on the spectrum shown in the right bottom panel of Fig. 4.

quadrature. The equispaced grid is essential in order to account for all transitions fulfilling $\mathbf{q} = \mathbf{G} + \mathbf{k}$. The discreteness of the mesh for \mathbf{k} and computational costs for a higher number of points make it difficult to represent the dispersion of excitation spectra as continuous functions of \mathbf{k} .

APPENDIX B: CORRESPONDENCE OF EXCITATIONS TO THE ENERGY BAND STRUCTURE OF THE DOT ARRAY

In the right panels of Fig. 4, and in Fig. 5 for $N_e = 2$ or 3, there appear many excitation peaks, especially around $\omega/\omega_c \approx 2$. These peaks reflect structures in the energy spectrum of the 2DEG. Here we will show the correspondence for the case of $pq = 3$ shown in the right panels of Fig. 4. The corresponding energy band structure is displayed in Fig. 10.

The excitation spectrum shown in the lower right panel of Fig. 4 is repeated in Fig. 11 for a narrower range for the frequency. The lowest energy band in Fig. 10 looks flat due to the effective localization of one electron in each dot, the higher bands show increasing dispersion that leads to several possible transitions or bands of transitions forming. The fact that $k_x L = k_y L = 0.785$ further complicates the excitation structure here

as it promotes not only dipole excitations. Actually, the lowest band has a regular structure not seen on the scale selected for the figure here. The transitions will have different strengths due to variations in the local density of states caused by local extrema of the bands. In addition, the matrix elements depend on their location in the magnetic Brillouin zone of reciprocal space $\boldsymbol{\theta}$ and the values for $k_x L$ and $k_y L$.

A comparison of the spectra in Figs. 10 and 11 shows that the lowest main peak in the excitation spectrum occurs for ω/ω_c slightly higher than 1.6, but the energy distance between the two lowest bands in Fig. 10 corresponds to ω/ω_c just over 1.0. This difference is the well known depolarization shift for collective oscillations. The small dispersion visible for the second energy band in Fig. 10 produces the splitting of this lowest peak that is caused by effects of the square symmetry of the dot lattice creeping in. Now it is clear that the complex structure in Fig. 10 for the third to the sixth bands is bound to lead to a complex structure of excitations that are not easily assigned to individual transitions when $k_x L = k_y L = 0.785$.

Here we have considered $pq = 3$ and seen how the dispersion of the energy bands increases for the higher bands. This behavior is more pronounced for lower magnetic flux pq , but a bit weaker for $pq = 4$.

-
- [1] T. Ando, A. B. Fowler, and F. Stern, Electronic properties of two-dimensional systems, *Rev. Mod. Phys.* **54**, 437 (1982).
 - [2] W. Kohn, Cyclotron resonance and de Haas-van Alphen oscillations of an interacting electron gas, *Phys. Rev.* **123**, 1242 (1961).
 - [3] T. Demel, D. Heitmann, P. Grambow, and K. Ploog, Far-infrared response of one-dimensional electronic systems in single- and two-layered quantum wires, *Phys. Rev. B* **38**, 12732 (1988).
 - [4] P. A. Maksym and T. Chakraborty, Quantum Dots in a Magnetic Field: Role of Electron-Electron Interactions, *Phys. Rev. Lett.* **65**, 108 (1990).
 - [5] D. Heitmann and J. P. Kotthaus, The spectroscopy of quantum dots, *Phys. Today* **46**, 56 (1993).
 - [6] V. Shikin, S. Nazin, D. Heitmann, and T. Demel, Dynamic response of quantum dots, *Phys. Rev. B* **43**, 11903 (1991).
 - [7] T. Demel, D. Heitmann, P. Grambow, and K. Ploog, Nonlocal Dynamic Response and Level Crossings in Quantum-Dot Structures, *Phys. Rev. Lett.* **64**, 788 (1990).
 - [8] V. Gudmundsson and R. R. Gerhardt, Self-consistent model of magnetoplasmons in quantum dots with nearly parabolic confinement potentials, *Phys. Rev. B* **43**, 12098 (1991).
 - [9] K. Bollweg, T. Kurth, D. Heitmann, V. Gudmundsson, E. Vasiliadou, P. Grambow, and K. Eberl, Detection of Compressible and Incompressible States in Quantum Dots and Antidots by Far-Infrared Spectroscopy, *Phys. Rev. Lett.* **76**, 2774 (1996).
 - [10] T. Darnhofer, M. Suhrke, and U. Rössler, Far-infrared response of quantum dots: Filling factor dependence at high magnetic fields, *Europhys. Lett.* **35**, 591 (1996).
 - [11] I. Magnúsdóttir and V. Gudmundsson, Influence of the shape of quantum dots on their far-infrared absorption, *Phys. Rev. B* **60**, 16591 (1999).
 - [12] V. Gudmundsson, A. Brataas, P. Grambow, B. Meurer, T. Kurth, and D. Heitmann, Bernstein modes in quantum wires and dots, *Phys. Rev. B* **51**, 17744 (1995).
 - [13] A. Brataas, V. Gudmundsson, A. G. Mal'shukov, and K. A. Chao, The evolution of Bernstein modes in quantum wires with increasing deviation from parabolic confinement, *J. Phys.: Condens. Matter* **8**, 4797 (1996).
 - [14] J. Dempsey, N. F. Johnson, L. Brey, and B. I. Halperin, Collective modes in quantum-dot arrays in magnetic fields, *Phys. Rev. B* **42**, 11708 (1990).
 - [15] C. Dahl, J. P. Kotthaus, H. Nickel, and W. Schlapp, Coulomb coupling in arrays of electron disks, *Phys. Rev. B* **46**, 15590 (1992).
 - [16] N. Kim and S. E. Ulloa, Collective modes in tunneling quantum-dot arrays, *Phys. Rev. B* **48**, 11987 (1993).
 - [17] R. Kotlyar, C. A. Stafford, and S. Das Sarma, Addition spectrum, persistent current, and spin polarization in coupled quantum dot arrays: Coherence, correlation, and disorder, *Phys. Rev. B* **58**, 3989 (1998).
 - [18] B. P. van Zyl, E. Zaremba, and D. A. W. Hutchinson, Magnetoplasmon excitations in arrays of circular and noncircular quantum dots, *Phys. Rev. B* **61**, 2107 (2000).
 - [19] R. Krahne, V. Gudmundsson, C. Heyn, and D. Heitmann, Far-infrared excitations below the Kohn mode: Internal motion in a quantum dot, *Phys. Rev. B* **63**, 195303 (2001).
 - [20] P. G. Harper, Single band motion of conduction electrons in a uniform magnetic field, *Proc. Phys. Soc. A* **68**, 874 (1955).
 - [21] M. Y. Azbel', Energy spectrum of a conduction electron in a magnetic field, *Zh. Eksp. Teor. Fiz.* **46**, 929 (1964) [*Sov. Phys. JETP* **19**, 634 (1964)].
 - [22] D. Langbein, The tight-binding and the nearly-free-electron approach to lattice electrons in external magnetic fields, *Phys. Rev.* **180**, 633 (1969).

- [23] R. D. Hofstadter, Energy levels and wave functions of Bloch electrons in rational and irrational magnetic fields, *Phys. Rev. B* **14**, 2239 (1976).
- [24] V. Gudmundsson and R. R. Gerhardts, Manifestation of the Hofstadter butterfly in far-infrared absorption, *Phys. Rev. B* **54**, R5223 (1996).
- [25] V. Gudmundsson and R. R. Gerhardts, Effects of screening on the Hofstadter butterfly, *Phys. Rev. B* **52**, 16744 (1995).
- [26] E. Anisimovas and P. Johansson, Butterfly-like spectra and collective modes of antidot superlattices in magnetic fields, *Phys. Rev. B* **60**, 7744 (1999).
- [27] R. Kubo, Statistical-mechanical theory of irreversible processes. I. General theory and simple applications to magnetic and conduction problems, *J. Phys. Soc. Jpn.* **12**, 570 (1957).
- [28] K.-D. Zhu and S.-W. Gu, Cyclotron resonance of magnetopolarons in a parabolic quantum dot in strong magnetic fields, *Phys. Rev. B* **47**, 12941 (1993).
- [29] U. Merkt, Cyclotron Resonance of Localized Electron Systems in the Magnetic Quantum Limit, *Phys. Rev. Lett.* **76**, 1134 (1996).
- [30] S.-H. Chen, The cyclotron resonance of impurity magnetopolarons in two-dimensional quantum dots for all coupling strengths, *Phys. E* **43**, 1007 (2011).
- [31] N. T. T. Nguyen and F. M. Peeters, Cyclotron resonance of a magnetic quantum dot, *Phys. Rev. B* **78**, 245311 (2008).
- [32] Y. A. Bychkov and G. Martinez, Magnetoplasmons and cyclotron resonance in a two-dimensional electron gas, *Phys. Rev. B* **72**, 195328 (2005).
- [33] C. Faugeras, G. Martinez, A. Riedel, R. Hey, K. J. Friedland, and Y. Bychkov, Evidence for magnetoplasmon character of the cyclotron resonance response of a two-dimensional electron gas, *Phys. Rev. B* **75**, 035334 (2007).
- [34] S. Syed, M. J. Manfra, Y. J. Wang, H. L. Stormer, and R. J. Molnar, Large splitting of the cyclotron-resonance line in $\text{Al}_x\text{Ga}_{1-x}\text{N}/\text{GaN}$ heterostructures, *Phys. Rev. B* **67**, 241304(R) (2003).
- [35] A. Kriisa, R. L. Samaraweera, M. S. Heimbeck, H. O. Everitt, C. Reichl, W. Wegscheider, and R. G. Mani, Cyclotron resonance in the high mobility GaAs/AlGaAs 2D electron system over the microwave, mm-wave, and terahertz-bands, *Sci. Rep.* **9**, 2409 (2019).
- [36] R. G. Mani, A. Kriisa, C. Reichl, and W. Wegscheider, Microwave resonance in a high-quality GaAs/AlGaAs two-dimensional electron system in the low-density and low-mobility condition, *Phys. Rev. B* **100**, 155301 (2019).
- [37] A. Arnold, R. Bosi, S. Jeschke, and E. Zorn, On global classical solutions of the time-dependent von Neumann equation for Hartree-Fock systems, [arXiv:math-ph/0305027](https://arxiv.org/abs/math-ph/0305027).
- [38] V. Gudmundsson, C.-S. Tang, and A. Manolescu, Nonadiabatic current generation in a finite width semiconductor ring, *Phys. Rev. B* **67**, 161301(R) (2003).
- [39] V. Gudmundsson, S. Hauksson, A. Johnsen, G. Reinisch, A. Manolescu, C. Besse, and G. Dujardin, Excitation of radial collective modes in a quantum dot: Beyond linear response, *Annal. Phys.* **526**, 235 (2014).
- [40] R. Ferrari, Two-dimensional electrons in a strong magnetic field: A basis for single-particle states, *Phys. Rev. B* **42**, 4598 (1990).
- [41] H. Silberbauer, Magnetic minibands in lateral semiconductor superlattice, *J. Phys. C* **4**, 7355 (1992).
- [42] R. de la Madrid, The role of the rigged Hilbert space in quantum mechanics, *Eur. J. Phys.* **26**, 287 (2005).
- [43] C. Dahl, J. P. Kotthaus, H. Nickel, and W. Schlapp, Magnetoplasma resonances in two-dimensional electron rings, *Phys. Rev. B* **48**, 15480 (1993).
- [44] C. Dahl, Plasmons in periodically modulated inversion layers, *Phys. Rev. B* **41**, 5763 (1990).
- [45] A. Puente, L. Serra, and V. Gudmundsson, Hartree-Fock dynamics in highly excited quantum dots, *Phys. Rev. B* **64**, 235324 (2001).
- [46] F. M. Peeters, Magneto-optics in parabolic quantum dots, *Phys. Rev. B* **42**, 1486 (1990).
- [47] I. B. Bernstein, Waves in a plasma in a magnetic field, *Phys. Rev.* **109**, 10 (1958).
- [48] M. Valin-Rodriguez, A. Puente, L. Serra, V. Gudmundsson, and A. Manolescu, Characterization of Bernstein modes in quantum dots, *Eur. Phys. J. B* **28**, 111 (2002).
- [49] D. C. Glatli, E. Y. Andrei, G. Deville, J. Poitrenaud, and F. I. B. Williams, Dynamical Hall Effect in a Two-Dimensional Classical Plasma, *Phys. Rev. Lett.* **54**, 1710 (1985).
- [50] B. A. Wilson, S. J. Allen, and D. C. Tsui, Evidence for a magnetic-field-induced Wigner glass in the two-dimensional electron system in Si inversion layers, *Phys. Rev. B* **24**, 5887 (1981).
- [51] C. Dahl, B. Jusserand, A. Izrael, J. Gérard, L. Ferlazzo, and B. Etienne, Plasmons in the modulated and confined 2DEG: A Raman scattering study, *Superlattices Microstruct.* **15**, 441 (1994).
- [52] C. Steinebach, C. Schüller, and D. Heitmann, Resonant Raman scattering of quantum dots, *Phys. Rev. B* **59**, 10240 (1999).
- [53] C. Steinebach, C. Schüller, and D. Heitmann, Single-particle-like states in few-electron quantum dots, *Phys. Rev. B* **61**, 15600 (2000).
- [54] E. G. Mishchenko, Raman scattering in a two-dimensional electron gas: Boltzmann equation approach, *Phys. Rev. B* **59**, 14892 (1999).